

*Citation for published version:*

Wang, G, Yan, T, Shen, J, Zhang, J, Shi, L & Zhang, D 2021, 'Beneficial synergy of adsorption-intercalation-conversion mechanisms in Nb<sub>2</sub>O<sub>5</sub>@nitrogen-doped carbon frameworks for promoted removal of metal ions via hybrid capacitive deionization', *Environmental Science: Nano*, vol. 8, no. 1, pp. 122-130.  
<https://doi.org/10.1039/d0en01003k>

*DOI:*

[10.1039/d0en01003k](https://doi.org/10.1039/d0en01003k)

*Publication date:*

2021

*Document Version*

Peer reviewed version

[Link to publication](#)

Environ. Sci.: Nano, 2021,8, 122-130

**University of Bath**

## **Alternative formats**

If you require this document in an alternative format, please contact:  
[openaccess@bath.ac.uk](mailto:openaccess@bath.ac.uk)

### **General rights**

Copyright and moral rights for the publications made accessible in the public portal are retained by the authors and/or other copyright owners and it is a condition of accessing publications that users recognise and abide by the legal requirements associated with these rights.

### **Take down policy**

If you believe that this document breaches copyright please contact us providing details, and we will remove access to the work immediately and investigate your claim.



# Beneficial Synergy of Adsorption-Intercalation-Conversion Mechanisms in Nb<sub>2</sub>O<sub>5</sub>@Nitrogen-Doped Carbon Frameworks for Promoted Removal of Metal Ions via Hybrid Capacitive Deionization

Received 00th January 20xx,  
Accepted 00th January 20xx

DOI: 10.1039/x0xx00000x

www.rsc.org/

Guizhi Wang<sup>†</sup>, Tingting Yan<sup>†</sup>, Junjie Shen<sup>‡</sup>, Jianping Zhang<sup>†</sup>, Liyi Shi<sup>†</sup>, and Dongsong Zhang<sup>\*†</sup>

Capacitive deionization (CDI) is an emerging water purification technology, but the ion adsorption capacity of traditional carbon-based CDI electrodes is still unsatisfactory. Herein, a novel faradaic electrode by anchoring Nb<sub>2</sub>O<sub>5</sub> nanoparticles on the nitrogen-doped carbon frameworks as anodes and activated carbon (AC) as cathodes in a hybrid capacitive deionization (HCDI) system was originally developed to capture Na<sup>+</sup> ions via the adsorption-intercalation-conversion mechanisms. The synergetic effects of nanostructure and carbon coating were beneficial to enhancing electrical conductivity and offering fast Na<sup>+</sup> ions diffusion pathways. Impressively, the HCDI system demonstrated an excellent ion adsorption capacity of 35.4 mg g<sup>-1</sup> in a 500 mg L<sup>-1</sup> NaCl solution at 1.2 V as well as stable regeneration ability. In situ Raman and ex situ XPS measurements unraveled that the mechanism of ions removal from water was the reversible redox reaction of Nb<sub>2</sub>O<sub>5</sub>. The new overall understanding of synergetic effects opens opportunities for the design of HCDI systems for efficient removal of metal ions from saline water.

## 1 Introduction

In recent decades, the shortage of clean water has become a global issue as a consequence of population growth and climate change.<sup>1-3</sup> Less than 3% of all water on earth is fresh water, and only 1.2% of all fresh water is surface water which can be directly utilized. With this limited amount usable fresh water, desalination of saline water and brackish water offers a promising solution to the supply of clean water.<sup>4,5</sup> Traditional desalination methods have been examined to remove ions from seawater efficiently. Unfortunately, some of the methods suffer from various drawbacks including massive energy consumption, high cost and significant environmental impact.<sup>6,7</sup> Therefore, it is imperative to develop cost-effective and eco-friendly desalination technologies as promising alternatives. Capacitive deionization (CDI) has gained increasing attention due to its unique advantages of low energy consumption, low cost, rapid regeneration, and environmentally harmlessness.<sup>8,9</sup>

When applying a low potential on the two electrodes, the ions in solution can be quickly adsorbed and harvested in the oppositely-charged electrodes. Thus, the clean water is obtained.<sup>10,11</sup>

The ion removal capacity of CDI is closely dependent on the electrode materials. Carbon-based materials, such as carbon aerogels, carbon nanotubes, activated carbon, mesoporous carbon, and reduced graphene, have been extensively explored as CDI electrode materials due to the advantages of high surface area, porous structure, and electrochemical stability.<sup>12-15</sup> Unfortunately, one of the major limitations of carbon-based materials is the unsatisfactory ion adsorption capacity.<sup>16,17</sup> In carbon-based electrodes, the ions removed from solution are reserved on the carbon surface based on the electric double layer (EDL) theory, in which the removal capacity is mainly determined by the pores and surface area. In addition, the co-ions effect would restrain more ions from gathering and cause adsorbed ions to easily return to the solution.<sup>18,19</sup> To overcome the drawback, hybrid capacitive deionization (HCDI) has been developed. HCDI systems consist of one carbon electrode and one faradaic electrode.<sup>20,21</sup> In general, anions (such as Cl<sup>-</sup> ions) are electrostatic adsorbed on the carbon-based materials. But cations (such as Na<sup>+</sup> ions) are not only removed by surface adsorption, but also captured through a charge transfer reaction.<sup>22,23</sup> Compared with those EDL-based electrodes, HCDI systems deliver higher ion removal capacity and faster ion removal rates.<sup>24,25</sup> The selection of faradic materials for HCDI systems usually favored those with substantially improved energy storage domains.<sup>26,27</sup> Back in

<sup>†</sup> State Key Laboratory of Advanced Special Steel, School of Materials Science and Engineering, International Joint Laboratory of Catalytic Chemistry, Research Center of Nano Science and Technology, Department of Chemistry, College of Sciences, Shanghai University, No.99 Shangda Road, Shanghai, 200444, China.

<sup>‡</sup> Department of Chemical Engineering, University of Bath, Bath BA2 7AY, UK.

\* E-mail: dszhang@shu.edu.cn; Tel: +86 21 66137152.

Electronic supplementary information (ESI) available: materials, structural characterization, electrochemical characterization, CDI test, SEM images, TEM images, Particle size distribution, SAED pattern, EDS, XRD pattern, N<sub>2</sub> adsorption-desorption isotherms, BJH pore size distribution plots, XPS spectra, Dynamic water contact angle analysis, CV curves, Specific capacitance, GCD curves, IR drop, plots of IAC vs. deionization time, Ragone plots, Comparison between AIAR and CR, Regeneration test, Elemental quantification, Fitted parameters in EIS, and comparison of IAC with other reported materials. See DOI: 10.1039/x0xx00000x

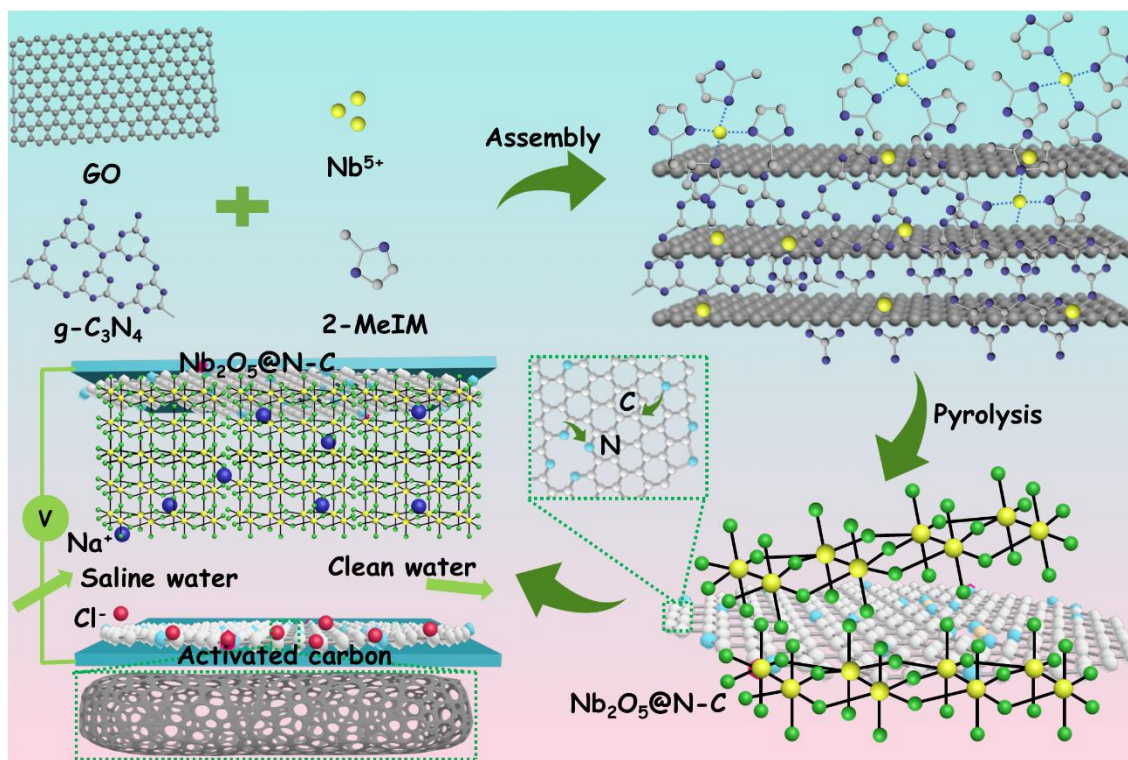


Figure 1. Schematic illustration of  $\text{Nb}_2\text{O}_5@\text{N-C}$  composites as anodes for hybrid capacitive deionization.

2012, Pasta<sup>28</sup> et al. selected  $\text{Na}_{2-x}\text{Mn}_5\text{O}_{10}$  and Ag as the electrodes and obtained good desalination performance. After that, a series of faradic electrode materials, such as  $\text{MnO}_2$ ,  $\text{TiO}_2$ ,  $\text{SnS}_2$ ,  $\text{MoS}_2$ ,  $\text{Na}_4\text{Ti}_9\text{O}_{20}$ ,  $\text{NaTi}_2(\text{PO}_4)_3$ , and Prussian blue, have been developed and proved to gain excellent ion removal capacities.<sup>29–32</sup> Wang<sup>33</sup> et al. used the hollow carbon@ $\text{MnO}_2$  to capture  $\text{Na}^+$  ions through redox reaction and obtained a high removal capacity of  $30.7 \text{ mg g}^{-1}$ . Our former work<sup>34</sup> synthesized  $\text{MoS}_2$ -graphene materials to reserve/convert  $\text{Na}^+$  ions via faradaic reaction. The obtained electrodes demonstrated a high volumetric adsorption capacity of  $14.3 \text{ mg cm}^{-3}$  in a  $500 \text{ mg L}^{-1}$  NaCl solution at 1.2 V.

Orthorhombic  $\text{Nb}_2\text{O}_5$  (T- $\text{Nb}_2\text{O}_5$ ), as a representative  $\text{Na}^+$  ions capture material with intercalation-conversion type, is a promising candidate HCDI electrode due to the intrinsic structural advantage.<sup>35, 36</sup> The (001) planes of  $\text{Nb}_2\text{O}_5$  has a larger interplanar spacing ( $3.9 \text{ \AA}$ ) than the size of  $\text{Na}^+$  ions ( $2.04 \text{ \AA}$ ), which may be suitable for  $\text{Na}^+$  ions diffusion.<sup>37</sup> Unfortunately, the low electrical conductivity ( $\approx 3 \times 10^{-6} \text{ S cm}^{-1}$ ) and the sluggish diffusion of  $\text{Na}^+$  ions from aggregation tendency may hinder the further application of  $\text{Nb}_2\text{O}_5$ . Two effective methods can be adopted to enhance the electrical conductivity and decrease the diffusion length for electrons/ions: (1) nanostructure engineering can turn the materials into low dimensions, which offers shorter pathways and faster  $\text{Na}^+$  ions diffusion;<sup>38, 39</sup> (2) composite with carbon can stabilize the materials and form an interconnected network for fast transport of electron and  $\text{Na}^+$  ions.<sup>40, 41</sup> Throughout all sorts of carbon-based supports, graphene gains much attention due to large surface area, good

chemical/physical stability, and superb electrical conductivity.<sup>42</sup> Moreover, the heteroatoms (such as nitrogen) doped in the carbon skeleton could boost electrical conductivity, introduce more defects, and improve hydrophilicity.<sup>43, 44</sup> Graphitic carbon nitride ( $\text{g-C}_3\text{N}_4$ ), as a suitable nitrogen precursor, has a relatively high nitrogen content of 57% and  $\text{sp}^2$  hybridized carbon structure. The high level of pyridine type nitrogen can offer abundant lone electron pairs to capture Nb atoms as benign ligands.<sup>45</sup> 2-Methylimidazole, as another benign N ligand, can coordinate with Nb and prohibit the large aggregation of  $\text{Nb}_2\text{O}_5$  nanocrystals during the heating process at elevated temperature.<sup>46</sup>

Herein, we originally designed  $\text{Nb}_2\text{O}_5$  anchored on nitrogen-doped carbon frameworks (denoted as  $\text{Nb}_2\text{O}_5@\text{N-C-1}$ ) via simple assembly and pyrolysis as anodes and activated carbon (AC) as cathodes. The obtained  $\text{Nb}_2\text{O}_5@\text{N-C-1}$  had uniform  $\text{Nb}_2\text{O}_5$  nanoparticles tightly anchored on the graphene networks. The N-doping improved the electrical conductivity and produced localized highly-reactive regions. Benefitting from the synergetic effects of structure optimization (nanostructure) and surface engineering (nitrogen-doped carbon coating), the  $\text{Nb}_2\text{O}_5@\text{N-C-1}$  electrode demonstrated superior CDI performance in terms of ion adsorption capacity and ion adsorption rates. Furthermore, in situ Raman and ex situ XPS analysis were conducted to verify the adsorption-intercalation-conversion mechanism of ion removal from water during the CDI process.

## 2 Materials and methods

First of all, graphene oxide (GO) was prepared by a modified Hummer's method,<sup>39</sup> and  $g\text{-C}_3\text{N}_4$  was obtained by a thermal decomposition/polymerization process.<sup>46</sup> Specifically, 0.02 g of GO and 0.1 g of  $g\text{-C}_3\text{N}_4$  were mixed in 50 mL of methanol after ultrasonic treatment for 1 h. Next, 0.11 g of  $\text{NbCl}_5$  was added into the mixture after ultrasonic treatment for 0.5 h to form solution Alpha. Meanwhile, 0.17 g of 2-Methylimidazole (2-MeIM) was dispersed in 30 mL of methanol after ultrasonic treatment for 0.5 h to form solution Beta. Then, solution Beta was dropwise added into solution Alpha with stirring, and the mixed solution was left at room temperature for 12 h. The  $\text{Nb}/2\text{MeIM}/g\text{-C}_3\text{N}_4/\text{GO}$  precursors were gained by centrifugation with methanol and drying at 60 °C for 12 h. After that, the dried material was calcined at 800 °C (3 °C/min) for 2 h under an  $\text{N}_2$  condition to obtain  $\text{Nb}_2\text{O}_5@N\text{-C-1}$  ( $\text{NbCl}_5$  and 2-MeIM with mole ratio of 1:1) composite. Simultaneously,  $\text{Nb}_2\text{O}_5@N\text{-C-2}$  (0.11 g of  $\text{NbCl}_5$  and 0.085 g of 2-MeIM with mole ratio of 2:1),  $\text{Nb}_2\text{O}_5@N\text{-C-0.5}$  (0.11 g of  $\text{NbCl}_5$  and 0.34 g of 2-MeIM with mole ratio of 1:2),  $\text{Nb}_2\text{O}_5$  (only utilization of  $\text{NbCl}_5$ ) and N-C (without utilization of  $\text{NbCl}_5$ ) were synthesized through similar procedure.

### 3 Results and discussion

#### 3.1 Characteristics Analysis

These  $\text{Nb}_2\text{O}_5@N\text{-C}$  composites were synthesized via an assembly approach followed by a pyrolysis method at 800 °C under a  $\text{N}_2$  condition, as shown in Figure 1. In the assembly process,  $\text{Nb}^{5+}$  ions were readily adsorbed on the surface of the negative charged  $\text{GO}/g\text{-C}_3\text{N}_4$  complex and further coordinated with 2-Methylimidazole (2-MeIM) to form the  $\text{Nb}/2\text{MeIM}/g\text{-C}_3\text{N}_4/\text{GO}$  precursors (Figure S1a, b). After the pyrolysis treatment, the  $\text{Nb}_2\text{O}_5@N\text{-C}$  composites were successfully prepared. The morphology and microstructure of the obtained samples were observed and verified by SEM and TEM (Figure S2). These electron microscopes images revealed that  $\text{Nb}_2\text{O}_5$  nanoparticles with an average size of around 50 nm (Figure S2c, S2f, and S2i) were tightly anchored on the nitrogen-doped graphene sheets. Besides, the density of  $\text{Nb}_2\text{O}_5$  nanocrystals

increased with the improvement of  $\text{Nb}^{5+}$  utilization, from  $\text{Nb}_2\text{O}_5@N\text{-C-0.5}$  (Figure S2a, b),  $\text{Nb}_2\text{O}_5@N\text{-C-1}$  (Figure S2d, e) to  $\text{Nb}_2\text{O}_5@N\text{-C-2}$  (Figure S2g, h). The contact between  $\text{Nb}_2\text{O}_5$  nanoparticles and graphene network (Figure 2a) could supply numerous pathways for ion diffusion and electron transfer, which would improve the electrochemical performance. The HRTEM image of  $\text{Nb}_2\text{O}_5@N\text{-C-1}$  (Figure 2b) displayed lattice fringes with a spacing of 0.393 nm, which were well attached to the (001) planes of the orthorhombic  $\text{Nb}_2\text{O}_5$  phase. In Figure S3, prominent diffraction rings were observed in the selected area electron diffraction (SAED) patterns, which confirmed the existence of (001), (180), and (200) planes of the orthorhombic  $\text{Nb}_2\text{O}_5$  phase. Furthermore, the relevant elemental mapping images of  $\text{Nb}_2\text{O}_5@N\text{-C-1}$  demonstrated uniform distributions of C, N, O, and Nb elements over the selected area, which proved that the  $\text{Nb}_2\text{O}_5$  nanoparticles were homogeneously anchored on the nitrogen-doped graphene networks (Figure S4).

The formation and crystalline structure of the  $\text{Nb}_2\text{O}_5$  nanocrystals in these  $\text{Nb}_2\text{O}_5@N\text{-C}$  composites were verified by the XRD analysis, as shown in Figure 2c and Figure S5. These characteristic diffraction peaks located at 22.6°, 25.7°, 28.4°, 28.9°, 36.6°, 37.0°, 46.2°, 50.9°, and 54.9°, could be appropriately indexed to (001), (041), (180), (200), (181), (201), (002), (331), and (371) planes of the orthorhombic  $\text{Nb}_2\text{O}_5$  phase (PDF#30-0873). To figure out the composition and structural properties of the correlative carbon supports, Raman analysis of the obtained samples was conducted (Figure 2d). Two typical carbon-based characteristic peaks of disordered carbon (D band) and  $\text{sp}^2$  bonded ordered graphitic carbon (G band) were observed at around 1350 and 1599  $\text{cm}^{-1}$ . The value of  $I_D/I_G$  was normally related to the degree of structural disorder and the number of defects. The  $I_D/I_G$  values of  $\text{Nb}_2\text{O}_5@N\text{-C-0.5}$ ,  $\text{Nb}_2\text{O}_5@N\text{-C-1}$ , and  $\text{Nb}_2\text{O}_5@N\text{-C-2}$  were 1.19, 1.16, and 1.11, revealing the abundant vacancies and defects. Moreover, the degree of disorder decreased with the increase of metal contents. Besides, the three small peaks at 121, 248, and 660  $\text{cm}^{-1}$  were the characteristic bands of  $\text{Nb}_2\text{O}_5$ , which corresponded to the vibrations of octahedrons, the bending vibration of Nb-O bond, and the stretching vibration of Nb-O bond,<sup>47, 48</sup> respectively. The pore structure characteristics of  $\text{Nb}_2\text{O}_5@N\text{-C}$  composites were obtained by  $\text{N}_2$  adsorption/desorption measurements. Both the BET specific surface area and pore volume decreased as the amount of  $\text{Nb}_2\text{O}_5$  in the composite increased (Table S1).  $\text{Nb}_2\text{O}_5@N\text{-C-0.5}$  gained the largest BET specific surface area of 78.6  $\text{m}^2 \text{g}^{-1}$ , in comparison of  $\text{Nb}_2\text{O}_5@N\text{-C-1}$  of 34.1  $\text{m}^2 \text{g}^{-1}$  and  $\text{Nb}_2\text{O}_5@N\text{-C-2}$  of 29.5  $\text{m}^2 \text{g}^{-1}$  (Figure S6a). Moreover, the pore size distribution plots indicated the mesoporous structures of the three samples, which could supply abundant diffusion channels for ions transportation. Specifically,  $\text{Nb}_2\text{O}_5@N\text{-C-1}$  showed a similar pore size and volume distribution compared to  $\text{Nb}_2\text{O}_5@N\text{-C-0.5}$ , much higher and richer than  $\text{Nb}_2\text{O}_5@N\text{-C-2}$  in the range of 2-10 nm (Figure S6b). To further investigate the surface chemical elements and bonding states of the  $\text{Nb}_2\text{O}_5@N\text{-C}$  composites, XPS analysis was conducted, as shown in Figure S7. The Nb 3d, C 1s, N 1s, and O 1s signals

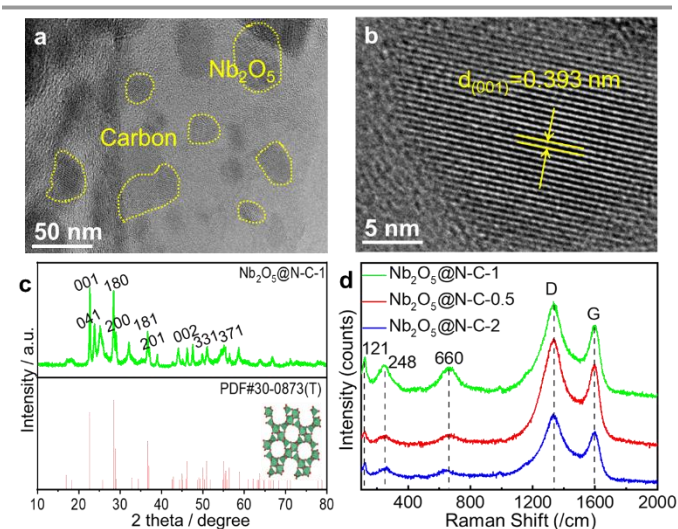


Figure 2. (a) TEM image, (b) HRTEM image, (c) XRD pattern of  $\text{Nb}_2\text{O}_5@N\text{-C-1}$ , and (d) Raman spectra of  $\text{Nb}_2\text{O}_5@N\text{-C-0.5}$ ,  $\text{Nb}_2\text{O}_5@N\text{-C-1}$ , and  $\text{Nb}_2\text{O}_5@N\text{-C-2}$ .

were obviously seen in the full-scan spectra of Nb<sub>2</sub>O<sub>5</sub>@N-C-0.5, Nb<sub>2</sub>O<sub>5</sub>@N-C-1, and Nb<sub>2</sub>O<sub>5</sub>@N-C-2, proving the successful integration of Nb<sub>2</sub>O<sub>5</sub> in the structure of carbon frameworks. Moreover, the formation of C-N bond (Figure S8) confirmed the insertion of N atoms into the carbon plane. The N 1s peak consisted of four types of N, namely pyridinic N, pyrrolic N, graphitic N, and oxide N (Figure S9). The Nb-O bond (Figure S10) verified the presence of Nb<sub>2</sub>O<sub>5</sub>. The atomic percentage of Nb element (Table S2) increased from Nb<sub>2</sub>O<sub>5</sub>@N-C-0.5 to Nb<sub>2</sub>O<sub>5</sub>@N-C-2, which was consistent with the Nb precursors utilization in the synthesis process. Since the electrochemical properties and CDI performance were tested in NaCl aqueous solution, the hydrophilicity of the electrode materials was also a vital indicator. We evaluated the hydrophilicity by dynamic water contact angle test (Figure S11). The results showed that Nb<sub>2</sub>O<sub>5</sub>@N-C-1 had a smaller contact angle (74.29°) than Nb<sub>2</sub>O<sub>5</sub>@N-C-0.5 (75.42°) and Nb<sub>2</sub>O<sub>5</sub>@N-C-2 (84.14°). The good hydrophilicity of Nb<sub>2</sub>O<sub>5</sub>@N-C-1 was due to the porous structure and abundant N content within the carbon frameworks.

### 3.2 Electrochemical Performance

The electrochemical performance of Nb<sub>2</sub>O<sub>5</sub>@N-C composites was firstly evaluated by cyclic voltammetry (CV). The CV plots were obtained at scan rates ranging from 1 to 100 mV s<sup>-1</sup> (Figure S12a-c). For every composite, the integrated area of CV curve was gradually enlarged with the increase of scan rates. At the same scan rate, the Nb<sub>2</sub>O<sub>5</sub>@N-C-1 curve had the largest integrated area, followed by the Nb<sub>2</sub>O<sub>5</sub>@N-C-0.5 and Nb<sub>2</sub>O<sub>5</sub>@N-C-2 curves. As a result, the Nb<sub>2</sub>O<sub>5</sub>@N-C-1 possessed the highest specific capacitance among these composites at any scan rate (Figure S12d). To gain a deeper insight into the charge transfer mechanisms in Nb<sub>2</sub>O<sub>5</sub>@N-C-1,

we quantitatively divided the contributions of capacitive and diffusion-controlled effects from CV plots by using a slower scan rate of 0.1 mV s<sup>-1</sup>. In Figure 3a, a redox peak appeared at around -0.13 V, demonstrating a faradic reaction of Na<sup>+</sup> ions inserting into the Nb<sub>2</sub>O<sub>5</sub>@N-C-1 electrode. Therefore, the Na<sup>+</sup> ions are removed by the synergetic effects of electro-adsorption of the nitrogen-doped carbon frameworks and faradaic reaction of Nb<sub>2</sub>O<sub>5</sub> (Figure S13). The surface capacitive (shade areas) and diffusion-controlled contributions of Nb<sub>2</sub>O<sub>5</sub>@N-C-1 at 0.1 mV s<sup>-1</sup> were 64.3% and 35.7%, respectively.<sup>37, 49</sup> The results confirmed that Nb<sub>2</sub>O<sub>5</sub> played a leading role in capturing Na<sup>+</sup> ions. Figure S14a-c indicated the galvanostatic charge-discharge (GCD) plots of Nb<sub>2</sub>O<sub>5</sub>@N-C-0.5, Nb<sub>2</sub>O<sub>5</sub>@N-C-1, and Nb<sub>2</sub>O<sub>5</sub>@N-C-2 at a current density of 0.2, 0.4, 0.6, 0.8, 1.0 and 1.2 A g<sup>-1</sup>. The GCD plots demonstrated analogous symmetric triangular shapes, exhibiting benign electrochemical reversibility. Besides, when the current density was raised from 0.2 to 1.2 A g<sup>-1</sup>, the Nb<sub>2</sub>O<sub>5</sub>@N-C-1 electrode showed the longest discharge time, which manifested the largest capacitance in accordance with the CV results. Additionally, Nb<sub>2</sub>O<sub>5</sub>@N-C-1 showed a lower potential drop (iR) than other materials at the initial discharge process (Figure S14d), suggesting a better electrical resistance. Cycling stability was another vital parameter for electrode materials. In Figure 3b, the GCD plots maintained the original shape after 10000 cycles at 10 A g<sup>-1</sup>, manifesting an outstanding cycle-to-cycle durability. The superior electrochemical property of Nb<sub>2</sub>O<sub>5</sub>@N-C-1 was further demonstrated by electrochemical impedance spectroscopy (EIS), as shown in Figure 3c. The Nyquist plots consisted of a semicircle in the medium frequency region corresponding to charge-transfer resistance (R<sub>ct</sub>), and a straight segment in the low frequency region corresponding to Warburg diffusion impedance (W). An equivalent circuit (inset of Figure 3c) was employed to simulate these EIS curves, in which R<sub>s</sub> and CPE<sub>ct</sub> represented solution resistance and constant phase part, respectively.<sup>50</sup> Nb<sub>2</sub>O<sub>5</sub>@N-C-1 demonstrated the smallest semicircle among the three electrodes, indicating the lowest charge-transfer impedance. According to the fitting results (Table S3), the R<sub>ct</sub> values were 14.66, 18.52, and 23.94 Ω for Nb<sub>2</sub>O<sub>5</sub>@N-C-1, Nb<sub>2</sub>O<sub>5</sub>@N-C-0.5, and Nb<sub>2</sub>O<sub>5</sub>@N-C-2, respectively. Furthermore, the diffusion coefficient (D<sub>Na<sup>+</sup></sub>) of Nb<sub>2</sub>O<sub>5</sub>@N-C-1 was 4.18×10<sup>-15</sup> cm<sup>2</sup> s<sup>-1</sup>, much larger than those of Nb<sub>2</sub>O<sub>5</sub>@N-C-0.5 (2.49×10<sup>-15</sup> cm<sup>2</sup> s<sup>-1</sup>) and Nb<sub>2</sub>O<sub>5</sub>@N-C-2 (2.27×10<sup>-15</sup> cm<sup>2</sup> s<sup>-1</sup>), indicating an enhanced Na<sup>+</sup> ions diffusion and adsorption (Figure 3d). Therefore, the excellent electrochemical properties may endow Nb<sub>2</sub>O<sub>5</sub>@N-C-1 with good CDI performance.

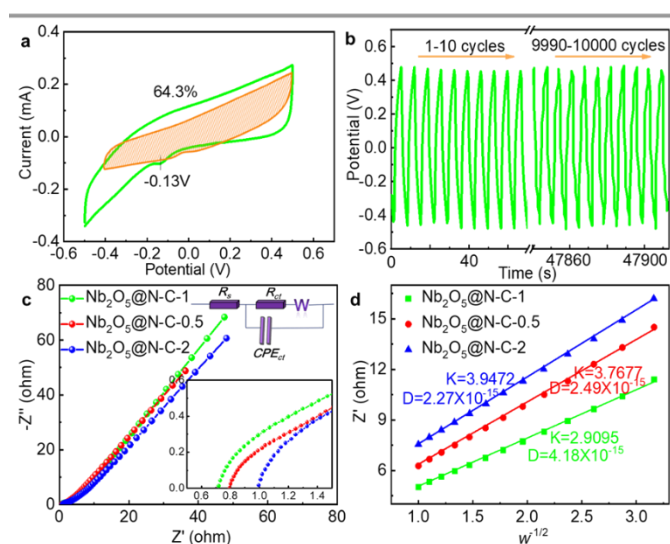


Figure 3. (a) Total current (green line) and capacitive current (shade regions) of Nb<sub>2</sub>O<sub>5</sub>@N-C-1 at 0.1 mV s<sup>-1</sup>, (b) 10000 GCD curves of Nb<sub>2</sub>O<sub>5</sub>@N-C-1 in the first 10 cycles and the last 10 cycles at 10 A g<sup>-1</sup>, (c) EIS of Nb<sub>2</sub>O<sub>5</sub>@N-C-0.5, Nb<sub>2</sub>O<sub>5</sub>@N-C-1, and Nb<sub>2</sub>O<sub>5</sub>@N-C-2, inset: the equivalent circuit to simulate EIS curves, and (d) The corresponding plots of real part impedance (Z') vs. squared root of the angular frequency ( $\omega^{-1/2}$ ) in the Warburg region.

### 3.3 Capacitive Deionization of Water

The batch-mode CDI experiments were conducted to evaluate the removal capacity of the electrode pairs. In Figure 4a, the deionization behaviors of Nb<sub>2</sub>O<sub>5</sub>//AC, Nb<sub>2</sub>O<sub>5</sub>@N-C-0.5//AC, Nb<sub>2</sub>O<sub>5</sub>@N-C-1//AC and Nb<sub>2</sub>O<sub>5</sub>@N-C-2//AC were analyzed in a 500 mg L<sup>-1</sup> NaCl solution at 1.2 V. It was observed that the ion adsorption capacity (IAC) increased quickly at first and then the trend is gradually slowdown within the required time. The Na<sup>+</sup> ions were removed through electro-adsorption

and electrochemical reactions with  $\text{Nb}_2\text{O}_5@N-C$ , while the negatively charged  $\text{Cl}^-$  ions were electrically-adsorbed by the AC electrode. After 120 min, the IAC of  $\text{Nb}_2\text{O}_5@N-C-1//AC$  reached  $35.4 \text{ mg g}^{-1}$ , much higher than those of  $\text{Nb}_2\text{O}_5@N-C-0.5//AC$ ,  $\text{Nb}_2\text{O}_5@N-C-2//AC$ , and  $\text{Nb}_2\text{O}_5//AC$  which were  $29.2 \text{ mg g}^{-1}$ ,  $19.4 \text{ mg g}^{-1}$ , and  $10.4 \text{ mg g}^{-1}$ , respectively. The result confirmed that the combinations of  $\text{Nb}_2\text{O}_5$  composite with nitrogen-doped carbon framework can enhance the removal capacity of pure metal oxides. In addition to IAC, the ion adsorption rate (IAR) is another key indicator of the CDI performance. Figure 4b showed the Ragone plots of IAR vs. IAC of the four electrodes. IAR was located at a high level firstly and moved downwards with the increase of IAC. The Ragone plot of  $\text{Nb}_2\text{O}_5@N-C-1//AC$  was located at the top right corner, suggesting that  $\text{Nb}_2\text{O}_5@N-C-1//AC$  had the fastest ion adsorption rate as well as the highest removal capacity among the four electrode materials. Additionally, to demonstrate the advantages of  $\text{Nb}_2\text{O}_5@N-C-1//AC$  over simple carbon substrate and the advantages of nitrogen-doped carbon framework over commercial AC, the desalination behavior of  $\text{Nb}_2\text{O}_5@N-C-1//AC$  along with  $N-C//AC$  and  $AC//AC$  were tested in a  $500 \text{ mg L}^{-1}$  NaCl solution at  $1.2 \text{ V}$ . Unsurprisingly, the  $\text{Nb}_2\text{O}_5@N-C-$

$1//AC$  composites exhibited the largest IAC and the quickest IAR (Figure S15). The outstanding performance of  $\text{Nb}_2\text{O}_5@N-C-1//AC$  was further confirmed in Figure S16 where  $\text{Nb}_2\text{O}_5@N-C-1//AC$  exhibited the greatest concentration reduction (CR) ( $0.88 \text{ mM}$ ) and the fastest average ion adsorption rate (AIAR) ( $0.50 \text{ mg g}^{-1} \text{ min}^{-1}$ ) among all the electrode materials. The charge utilization and energy loss in the CDI process could be measured by charge efficiency. The charge efficiencies of  $\text{Nb}_2\text{O}_5@N-C-0.5//AC$ ,  $\text{Nb}_2\text{O}_5@N-C-1//AC$ ,  $\text{Nb}_2\text{O}_5@N-C-2//AC$ , and  $\text{Nb}_2\text{O}_5//AC$  were calculated using the current transient curves in a  $500 \text{ mg L}^{-1}$  NaCl solution at  $1.2 \text{ V}$ . As shown in Figure 4c,  $\text{Nb}_2\text{O}_5@N-C-1//AC$  had a higher charge efficiency ( $0.70$ ) than  $\text{Nb}_2\text{O}_5@N-C-0.5//AC$  ( $0.58$ ),  $\text{Nb}_2\text{O}_5@N-C-2//AC$  ( $0.46$ ) and  $\text{Nb}_2\text{O}_5//AC$  ( $0.31$ ). A series of trade-off curves between the inverse of specific energy consumption ( $\text{SEC}^{-1}$ ) and IAR were also recorded in a  $500 \text{ mg L}^{-1}$  NaCl solution at  $1.2 \text{ V}$ . In Figure 4d, the trade-off curve of  $\text{Nb}_2\text{O}_5@N-C-1//AC$  was always above the curves of  $\text{Nb}_2\text{O}_5@N-C-0.5//AC$ ,  $\text{Nb}_2\text{O}_5@N-C-2//AC$ , and  $\text{Nb}_2\text{O}_5//AC$ . This means  $\text{Nb}_2\text{O}_5@N-C-1//AC$  reached the fastest IAR in the same  $\text{SEC}^{-1}$  compared with other electrodes, demonstrating the most efficient energy utilization. The synergetic effects of electro-adsorption of nitrogen-doped carbon framework and faradaic reaction of  $\text{Nb}_2\text{O}_5$  facilitated ion diffusion and ions adsorption. The deionization property of  $\text{Nb}_2\text{O}_5@N-C-1//AC$  was further analyzed at various initial concentrations of NaCl solution and different applied voltages. In Figure 4e, it was clear that the IAC of  $\text{Nb}_2\text{O}_5@N-C-1//AC$  increased from  $18.1$ ,  $27.4$ , to  $35.4 \text{ mg g}^{-1}$  as the NaCl concentrations increased from  $100$ ,  $300$ , to  $500 \text{ mg L}^{-1}$  at  $1.2 \text{ V}$ . In general, a higher NaCl concentration reduced the ionic resistance and facilitated fast ion adsorption. Compared with other reported metal-based electrode materials (Table S4),  $\text{Nb}_2\text{O}_5@N-C-1$  exhibited excellent deionization behavior with high ion adsorption capacity. Moreover, the Ragone plot moved to the top right with the increase of NaCl concentration, verifying a faster IAR and a higher IAC in a  $500 \text{ mg L}^{-1}$  solution (Figure S17a). Figure 4f presented the IAC of  $\text{Nb}_2\text{O}_5@N-C-1//AC$  at distinct applied voltages of  $0.8$ ,  $1.0$ , and  $1.2 \text{ V}$ . The change of voltages was consistent with the change of NaCl concentrations. Notably, IAC increased from  $4.9$ ,  $19.1$ , to  $35.4 \text{ mg g}^{-1}$  when the voltage was raised from  $0.8$ ,  $1.0$ , to  $1.2 \text{ V}$ . The Ragone plots (Figure S17b) also showed a faster IAR and a higher IAC at a higher voltage. The enhanced deionization performance was due to the stronger electrostatic force at a higher applied voltage. The comparison between CR and AIAR in different combinations of NaCl concentration and voltage also showed that the best performance was achieved when the initial NaCl concentration was  $500 \text{ mg L}^{-1}$  and the applied voltage was  $1.2 \text{ V}$  (Figure S18). The regeneration ability was crucial to justifying a deionization material for further applications. The continuous cyclic adsorption-desorption experiments of  $\text{Nb}_2\text{O}_5@N-C-1//AC$  were conducted in a  $100 \text{ mg L}^{-1}$  NaCl solution (Figure S19). The adsorption process was started by applying a  $1.2 \text{ V}$  voltage, and the subsequent desorption process was realized by short circuiting at  $0 \text{ V}$ . In every cycle, the electrical conductivity dropped to a low level during the adsorption process and recovered to the initial level

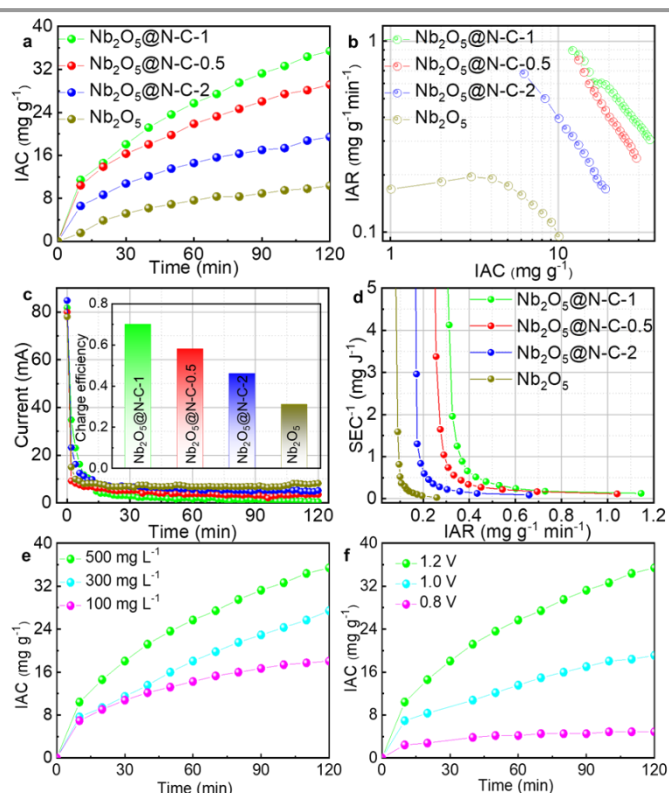


Figure 4. (a) IAC plots of  $\text{Nb}_2\text{O}_5$ ,  $\text{Nb}_2\text{O}_5@N-C-0.5$ ,  $\text{Nb}_2\text{O}_5@N-C-1$ , and  $\text{Nb}_2\text{O}_5@N-C-2$  electrodes in a  $500 \text{ mg L}^{-1}$  NaCl solution with a working voltage of  $1.2 \text{ V}$  and flow rate of  $40 \text{ mL min}^{-1}$ , (b) The corresponding Ragone plots of IAR vs. IAC of the three electrodes, (c) Current transient curves and charge efficiency (insert figure) of  $\text{Nb}_2\text{O}_5$ ,  $\text{Nb}_2\text{O}_5@N-C-0.5$ ,  $\text{Nb}_2\text{O}_5@N-C-1$ , and  $\text{Nb}_2\text{O}_5@N-C-2$  electrodes in a  $500 \text{ mg L}^{-1}$  NaCl solution with a working voltage of  $1.2 \text{ V}$  and flow rate of  $40 \text{ mL min}^{-1}$ , (d) Plots of the trade-off between  $\text{SEC}^{-1}$  and SAR of  $\text{Nb}_2\text{O}_5$ ,  $\text{Nb}_2\text{O}_5@N-C-0.5$ ,  $\text{Nb}_2\text{O}_5@N-C-1$ , and  $\text{Nb}_2\text{O}_5@N-C-2$  electrode materials, (e) IAC plots of  $\text{Nb}_2\text{O}_5@N-C-1$  in a different initial concentration of NaCl solution with a working voltage of  $1.2 \text{ V}$  and flow rate of  $40 \text{ mL min}^{-1}$ , (f) IAC plots of  $\text{Nb}_2\text{O}_5@N-C-1$  in a  $500 \text{ mg L}^{-1}$  NaCl solution with different working voltage and flow rate of  $40 \text{ mL min}^{-1}$ .

during the desorption process. The water recovery (WR) was 33.3%, the energy consumption was  $100 \text{ J g}^{-1}$  and energy efficiency was 19.58% under same measurement condition in one cycle. The deionization rate demonstrated general stability over 20 consecutive adsorption-desorption cycles. After the regeneration test, the  $\text{Nb}_2\text{O}_5$  nanoparticles were still tightly anchored on the nitrogen-doped graphene sheets (Figure S20a, b). But the size of  $\text{Nb}_2\text{O}_5$  nanoparticles slightly decreased, which could shorten ion transport pathways and provide rapid diffusion channels in a long-term operation (Figure S20c). The above results proved that  $\text{Nb}_2\text{O}_5@\text{N-C-1}$  possessed outstanding regeneration ability.

### 3.4 Mechanisms of Ions Removal

The mechanisms of ions removal from water were investigated by in situ Raman characterization. Figure 5a recorded the in-situ Raman spectra when the CV plots (scan rate of  $0.1 \text{ mV s}^{-1}$ ) reached to different stages of ion adsorption and desorption (Figure S21). During the ion adsorption process from 0.5 to -0.5 V, the evolution of each band could be summarized as follows. (1) the  $V_{\text{Hi}}$  band kept nearly constant from 0.5 to 0.1 V. When the potential decreased to -0.1 V, the  $V_{\text{Hi}}$  band demonstrated a red shift and the relative intensity increased, which was consistent with the CV curves in which a prominent cathodic peak appeared at this range. (2) the  $V_{\text{Mid}}$  band presented a similar trend with the  $V_{\text{Hi}}$  band. No noticeable change was observed from 0.5 to 0.1 V. After that, the  $V_{\text{Mid}}$  band split into two small bands from -0.1 to -0.5 V. (3) the  $V_{\text{Lo}}$  band, after being static at the range from 0.5 to 0.1 V, demonstrated an increased relative intensity from -0.1 V. In contrast, the evolution of the three bands in  $\text{Na}^+$  ions deintercalation process was the exact opposite of the above-mentioned  $\text{Na}^+$  ions intercalation. Specifically, during the ion desorption process from -0.5 to 0.5 V, the  $V_{\text{Hi}}$  band was blue-

one band; and the  $V_{\text{Lo}}$  band also decreased in intensity. The opposite evolutions of these Raman band groups of  $\text{Nb}_2\text{O}_5$  verified the reversible structural conversion via  $\text{Na}^+$  ions intercalation/deintercalation.<sup>51, 52</sup> Moreover, ex situ XPS analysis was used to observe the valence changes in Nb element during the ion adsorption and ion desorption process. As shown in Figure S22, there was a clear blue shift from the pristine state to the adsorption state and the subsequent red shift from the adsorption state to the desorption state. The reversible shift of Nb  $3d_{5/2}$  and Nb  $3d_{3/2}$  revealed that the valence changes of Nb had a strong correlation with the  $\text{Na}^+$  ions conversion process. The Nb 3d XPS spectra of the three states were divided into individual peaks to provide more information about the removal mechanisms (Figure 5b). At the pristine state,  $\text{Nb}^{5+}$  played a significant role while  $\text{Nb}^{4+}$  was in the minority. After that, the majority of  $\text{Nb}^{5+}$  were reduced into  $\text{Nb}^{4+}$  when the electrode adsorbed sufficient  $\text{Na}^+$  ions. Finally, most  $\text{Nb}^{4+}$  were oxidized to  $\text{Nb}^{5+}$  after the applied voltage was removed. The above XPS results indicated that the  $\text{Na}^+$  ions conversion process arose from the reversible redox reaction of the  $\text{Nb}^{5+}/\text{Nb}^{4+}$  pair in the  $\text{Nb}_2\text{O}_5@\text{N-C-1}$  electrode.<sup>53-55</sup> The  $\text{Na}^+$  ions insertion/extraction reaction could be expressed as  $\text{Nb}_2\text{O}_5 + x \text{ Na}^+ + x \text{ e}^- \rightleftharpoons \text{Na}_x\text{Nb}_2\text{O}_5$ .<sup>38, 53</sup> Meanwhile,  $\text{Cl}^-$  ions were adsorbed on the surface of the positively charged AC during the ion adsorption process, and released back to the salt solution during the ion desorption process. Therefore, the removal mechanisms of  $\text{Na}^+$  ion and  $\text{Cl}^-$  ion could be distinctly illustrated in Figure 5c.

## 4 Conclusions

In summary, the exceptional CDI performance of  $\text{Nb}_2\text{O}_5@\text{N-C-1}$  could be explained by the synergetic effects of electro-adsorption of nitrogen-doped carbon framework and faradaic reaction of  $\text{Nb}_2\text{O}_5$ . GO, g- $\text{C}_3\text{N}_4$  and 2-MeIM derived nitrogen-

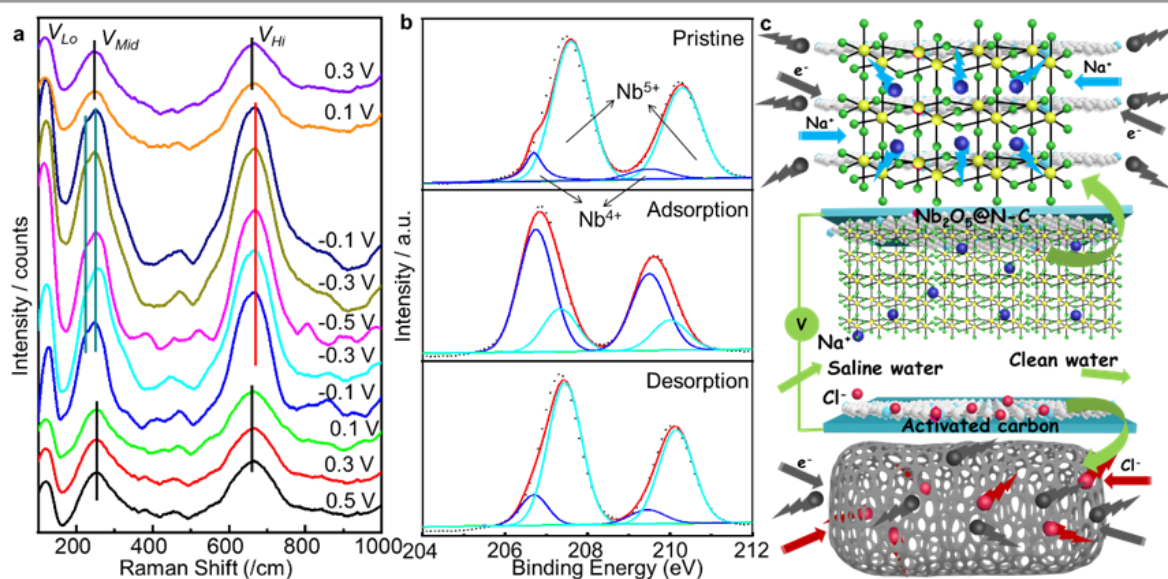


Figure 5. (a) In-situ Raman tests of  $\text{Na}^+$  ions adsorption/desorption behavior in  $\text{Nb}_2\text{O}_5@\text{N-C-1}$ , (b) The corresponding valence change of Nb during the pristine, adsorption, and desorption process, and (c) Schematic illustration of ions removal mechanisms in  $\text{Nb}_2\text{O}_5@\text{N-C-1}$ .

shifted with a reduced intensity; the  $V_{\text{Mid}}$  bands merged into doped carbon (N-C) as the flexible support showed superb

cycling stability. Besides, the introduction of N-C enhanced the electrical conductivity of Nb<sub>2</sub>O<sub>5</sub> and realized a better Na<sup>+</sup> ions diffusion. Nb<sub>2</sub>O<sub>5</sub> in-situ growth on the N-C framework increased the ion diffusion channels and facilitated the fast transport of Na<sup>+</sup> ion. Owing to the combination of electro-adsorption/desorption mechanism of N-C and insertion/extraction process of Nb<sub>2</sub>O<sub>5</sub>, the Nb<sub>2</sub>O<sub>5</sub>@N-C-1 electrode displayed an excellent ion removal capacity. Inspiringly, the novel HCEDI system equipped with Nb<sub>2</sub>O<sub>5</sub>@N-C-1//AC exhibited superb IAC (35.4 mg g<sup>-1</sup> in a 500 mg L<sup>-1</sup> NaCl solution at 1.2 V), fast IAR, high charge efficiency, low energy loss, and good regeneration ability. In situ Raman and ex situ XPS analysis verified that the mechanisms of ions removal were reversible intercalation and faradaic reaction of Nb<sub>2</sub>O<sub>5</sub>. This work presents a new strategy to design highly efficient HCEDI systems for water purification.

### Conflicts of interest

There are no conflicts to declare.

### Acknowledgements

The authors acknowledge the support of the National Natural Science Foundation of China (21906101; 21722704) and the Science and Technology Commission of Shanghai Municipality (19DZ2293100; 18DZ2281400).

### Notes and references

1. T. Oki and S. Kanae, *Global Hydrological Cycles and World Water Resources*, Science, 2006, 313, 1068.
2. C. J. Vörösmarty, P. B. McIntyre, M. O. Gessner, D. Dudgeon, A. Prusevich, P. Green, S. Glidden, S. E. Bunn, C. A. Sullivan, C. R. Liermann and P. M. Davies, *Global threats to human water security and river biodiversity*, Nature, 2010, 467, 555-561.
3. G. Wang, T. Yan, J. Zhang, L. Shi and D. Zhang, *Trace-Fe-Enhanced Capacitive Deionization of Saline Water by Boosting Electron Transfer of Electro-Adsorption Sites*, Environ. Sci. Technol., 2020, 54, 8411-8419.
4. J.-F. Pekel, A. Cottam, N. Gorelick and A. S. Belward, *High-resolution mapping of global surface water and its long-term changes*, Nature, 2016, 540, 418-422.
5. M. Elimelech and W. A. Phillip, *The Future of Seawater Desalination: Energy, Technology, and the Environment*, Science, 2011, 333, 712.
6. J. E. Dykstra, R. Zhao, P. M. Biesheuvel and A. van der Wal, *Resistance identification and rational process design in Capacitive Deionization*, Water Res., 2016, 88, 358-370.
7. C. Zhang, D. He, J. Ma, W. Tang and T. D. Waite, *Faradaic reactions in capacitive deionization (CDI)-problems and possibilities: A review*, Water Res., 2018, 128, 314-330.
8. S. P. Surwade, S. N. Smirnov, I. V. Vlasiouk, R. R. Unocic, G. M. Veith, S. Dai and S. M. Mahurin, *Water desalination using nanoporous single-layer graphene*, Nature Nanotechnol., 2015, 10, 459-464.
9. C. He, J. Ma, C. Zhang, J. Song and T. D. Waite, *Short-Circuited Closed-Cycle Operation of Flow-Electrode CDI for Brackish Water Softening*, Environ. Sci. Technol., 2018, 52, 9350-9360.
10. P. Liu, T. Yan, L. Shi, H. S. Park, X. Chen, Z. Zhao and D. Zhang, *Graphene-based materials for capacitive deionization*, J. Mater. Chem. A, 2017, 5, 13907-13943.
11. T. Wang, C. Zhang, L. Bai, B. Xie, Z. Gan, J. Xing, G. Li and H. Liang, *Scaling behavior of iron in capacitive deionization (CDI) system*, Water Res., 2020, 171, 115370.
12. J. Zhang, T. Yan, J. Fang, J. Shen, L. Shi and D. Zhang, *Enhanced capacitive deionization of saline water using N-doped rod-like porous carbon derived from dual-ligand metal-organic frameworks*, Environ. Sci.: Nano, 2020, 7, 926-937.
13. Z. U. Khan, T. Yan, J. Han, L. Shi and D. Zhang, *Capacitive deionization of saline water using graphene nanosphere decorated N-doped layered mesoporous carbon frameworks*, Environ. Sci.: Nano, 2019, 6, 3442-3453.
14. W. Tang, J. Liang, D. He, J. Gong, L. Tang, Z. Liu, D. Wang and G. Zeng, *Various cell architectures of capacitive deionization: Recent advances and future trends*, Water Res., 2019, 150, 225-251.
15. F. Ji, L. Wang, J. Yang, X. Wu, M. Li, S. Jiang, S. Lin and Z. Chen, *Highly compact, free-standing porous electrodes from polymer-derived nanoporous carbons for efficient electrochemical capacitive deionization*, J. Mater. Chem. A, 2019, 7, 1768-1778.
16. Y.-W. Chen, J.-F. Chen, C.-H. Lin and C.-H. Hou, *Integrating a supercapacitor with capacitive deionization for direct energy recovery from the desalination of brackish water*, Appl. Energy, 2019, 252, 113417.
17. F. Yu, L. Wang, Y. Wang, X. Shen, Y. Cheng and J. Ma, *Faradaic reactions in capacitive deionization for desalination and ion separation*, J. Mater. Chem. A, 2019, 7, 15999-16027.
18. J. Cao, Y. Wang, L. Wang, F. Yu and J. Ma, *Na<sub>3</sub>V<sub>2</sub>(PO<sub>4</sub>)<sub>3</sub>@C as Faradaic Electrodes in Capacitive Deionization for High-Performance Desalination*, Nano Lett., 2019, 19, 823-828.
19. L. Wang, J. E. Dykstra and S. Lin, *Energy Efficiency of Capacitive Deionization*, Environ. Sci. Technol., 2019, 53, 3366-3378.
20. M. Li and H. G. Park, *Pseudocapacitive Coating for Effective Capacitive Deionization*, ACS Appl. Mater. Interfaces, 2018, 10, 2442-2450.
21. F. Zhou, T. Gao, M. Luo and H. Li, *Heterostructured graphene@Na<sub>4</sub>Ti<sub>9</sub>O<sub>20</sub> nanotubes for asymmetrical capacitive deionization with ultrahigh desalination capacity*, Chem. Eng. J., 2018, 343, 8-15.
22. F. Xing, T. Li, J. Li, H. Zhu, N. Wang and X. Cao, *Chemically exfoliated MoS<sub>2</sub> for capacitive deionization of saline water*, Nano Energy, 2017, 31, 590-595.
23. Y. Zhao, B. Liang, X. Wei, K. Li, C. Lv and Y. Zhao, *A core-shell heterostructured CuFe@NiFe Prussian blue analogue as a novel electrode material for high-capacity and stable capacitive deionization*, J. Mater. Chem. A, 2019, 7, 10464-10474.
24. K. Wang, Y. Liu, Z. Ding, Y. Li, T. Lu and L. Pan, *Metal-organic-frameworks-derived NaTi<sub>2</sub>(PO<sub>4</sub>)<sub>3</sub>/carbon composites for efficient hybrid capacitive deionization*, J. Mater. Chem. A, 2019, 7, 12126-12133.
25. Z. Yue, T. Gao and H. Li, *Robust synthesis of carbon@Na<sub>4</sub>Ti<sub>9</sub>O<sub>20</sub> core-shell nanotubes for hybrid capacitive deionization with enhanced performance*, Desalination, 2019, 449, 69-77.
26. B. W. Byles, D. A. Cullen, K. L. More and E. Pomerantseva, *Tunnel structured manganese oxide nanowires as redox active electrodes for hybrid capacitive deionization*, Nano Energy, 2018, 44, 476-488.
27. W. Peng, W. Wang, G. Han, Y. Huang and Y. Zhang, *Fabrication of 3D flower-like MoS<sub>2</sub>/graphene composite as high-performance electrode for capacitive deionization*, Desalination, 2020, 473, 114191.



28. M. Pasta, C. D. Wessells, Y. Cui and F. La Mantia, A Desalination Battery, *Nano Lett.*, 2012, 12, 839-843.
29. Z. Y. Leong and H. Y. Yang, A Study of MnO<sub>2</sub> with Different Crystalline Forms for Pseudocapacitive Desalination, *ACS Appl. Mater. Interfaces*, 2019, 11, 13176-13184.
30. X. Wen, M. Zhao, M. Zhang, X. Fan and D. Zhang, Efficient Capacitive Deionization of Saline Water by an Integrated Tin disulfide Nanosheet@Graphite Paper Electrode via an In Situ Growth Strategy, *ACS Sustain. Chem. Eng.*, 2019, 8, 1268-1275.
31. M. Ding, S. Fan, S. Huang, M. E. Pam, L. Guo, Y. Shi and H. Y. Yang, Tunable Pseudocapacitive Behavior in Metal-Organic-Framework-Derived TiO<sub>2</sub>@Porous Carbon Enabling High-Performance Membrane Capacitive Deionization, *ACS Appl. Energy Mater.*, 2019, 2, 1812-1822.
32. B. H. Min, J.-H. Choi and K. Y. Jung, Improved capacitive deionization of sulfonated carbon/titania hybrid electrode, *Electrochim. Acta*, 2018, 270, 543-551.
33. S. Wang, G. Wang, T. Wu, C. Li, Y. Wang, X. Pan, F. Zhan, Y. Zhang, S. Wang and J. Qiu, Membrane-Free Hybrid Capacitive Deionization System Based on Redox Reaction for High-Efficiency NaCl Removal, *Environ. Sci. Technol.*, 2019, 53, 6292-6301.
34. J. Han, T. Yan, J. Shen, L. Shi, J. Zhang and D. Zhang, Capacitive Deionization of Saline Water by Using MoS<sub>2</sub>-Graphene Hybrid Electrodes with High Volumetric Adsorption Capacity, *Environ. Sci. Technol.*, 2019, 53, 12668-12676.
35. B. Deng, T. Lei, W. Zhu, L. Xiao and J. Liu, In-Plane Assembled Orthorhombic Nb<sub>2</sub>O<sub>5</sub> Nanorod Films with High-Rate Li<sup>+</sup> Intercalation for High-Performance Flexible Li-Ion Capacitors, *Adv. Funct. Mater.*, 2018, 28, 1704330.
36. P. Guo, K. Sun, X. Shang, D. Liu, Y. Wang, Q. Liu, Y. Fu and D. He, Nb<sub>2</sub>O<sub>5</sub>/RGO Nanocomposite Modified Separators with Robust Polysulfide Traps and Catalytic Centers for Boosting Performance of Lithium-Sulfur Batteries, *Small*, 2019, 15, e1902363.
37. X. Wang, Q. Li, L. Zhang, Z. Hu, L. Yu, T. Jiang, C. Lu, C. Yan, J. Sun and Z. Liu, Caging Nb<sub>2</sub>O<sub>5</sub> Nanowires in PECVD-Derived Graphene Capsules toward Bendable Sodium-Ion Hybrid Supercapacitors, *Adv. Mater.*, 2018, 30, e1800963.
38. D. Cao, Z. Yao, J. Liu, J. Zhang and C. Li, H-Nb<sub>2</sub>O<sub>5</sub> wired by tetragonal tungsten bronze related domains as high-rate anode for Li-ion batteries, *Energy Storage Mater.*, 2018, 11, 152-160.
39. G.-Z. Wang, J.-M. Feng, L. Dong, X.-F. Li and D.-J. Li, Antimony (IV) Oxide Nanorods/Reduced Graphene Oxide as the Anode Material of Sodium-ion Batteries with Excellent Electrochemical Performance, *Electrochim. Acta*, 2017, 240, 203-214.
40. K. Tang, T. Z. X. Hong, L. You and K. Zhou, Carbon-metal compound composite electrodes for capacitive deionization: synthesis, development and applications, *J. Mater. Chem. A*, 2019, 7, 26693-26743.
41. B. W. Byles, B. Hayes-Oberst and E. Pomerantseva, Ion Removal Performance, Structural/Compositional Dynamics, and Electrochemical Stability of Layered Manganese Oxide Electrodes in Hybrid Capacitive Deionization, *ACS Appl. Mater. Interfaces*, 2018, 10, 32313-32322.
42. J. Han, L. Shi, T. Yan, J. Zhang and D. Zhang, Removal of ions from saline water using N, P co-doped 3D hierarchical carbon architectures via capacitive deionization, *Environ. Sci.: Nano*, 2018, 5, 2337-2345.
43. J. Zhang, J. Fang, J. Han, T. Yan, L. Shi and D. Zhang, N, P, S co-doped hollow carbon polyhedra derived from MOF-based core-shell nanocomposites for capacitive deionization, *J. Mater. Chem. A*, 2018, 6, 15245-15252.
44. P. Liu, H. Wang, T. Yan, J. Zhang, L. Shi and D. Zhang, Grafting sulfonic and amine functional groups on 3D graphene for improved capacitive deionization, *J. Mater. Chem. A*, 2016, 4, 5303-5313.
45. R. Wang, T. Yan, L. Han, G. Chen, H. Li, J. Zhang, L. Shi and D. Zhang, Tuning the dimensions and structures of nitrogen-doped carbon nanomaterials derived from sacrificial g-C<sub>3</sub>N<sub>4</sub>/metal-organic frameworks for enhanced electrocatalytic oxygen reduction, *J. Mater. Chem. A*, 2018, 6, 5752-5761.
46. G. Wang, J. Deng, T. Yan, J. Zhang, L. Shi and D. Zhang, Turning on electrocatalytic oxygen reduction by creating robust Fe-N<sub>x</sub> species in hollow carbon frameworks via in situ growth of Fe doped ZIFs on g-C<sub>3</sub>N<sub>4</sub>, *Nanoscale*, 2020, 12, 5601-5611.
47. Q. Deng, F. Chen, S. Liu, A. Bayaguud, Y. Feng, Z. Zhang, Y. Fu, Y. Yu and C. Zhu, Advantageous Functional Integration of Adsorption-Intercalation-Conversion Hybrid Mechanisms in 3D Flexible Nb<sub>2</sub>O<sub>5</sub>@Hard Carbon@MoS<sub>2</sub>@Soft Carbon Fiber Paper Anodes for Ultrafast and Super-Stable Sodium Storage, *Adv. Funct. Mater.*, 2020, 30, 1908665.
48. X. Jiao, Q. Hao, X. Xia, Z. Wu and W. Lei, Metal organic framework derived Nb<sub>2</sub>O<sub>5</sub>@C nanoparticles grown on reduced graphene oxide for high-energy lithium ion capacitors, *Chem. Commun.*, 2019, 55, 2692-2695.
49. H. Kim, E. Lim, C. Jo, G. Yoon, J. Hwang, S. Jeong, J. Lee and K. Kang, Ordered-mesoporous Nb<sub>2</sub>O<sub>5</sub>/carbon composite as a sodium insertion material, *Nano Energy*, 2015, 16, 62-70.
50. Q. Ji, X. Gao, Q. Zhang, L. Jin, D. Wang, Y. Xia, S. Yin, S. Xia, N. Hohn, X. Zuo, X. Wang, S. Xie, Z. Xu, L. Ma, L. Chen, G. Z. Chen, J. Zhu, B. Hu, P. Müller - Buschbaum, P. G. Bruce and Y. J. Cheng, Dental Resin Monomer Enables Unique NbO<sub>2</sub>/Carbon Lithium-Ion Battery Negative Electrode with Exceptional Performance, *Adv. Funct. Mater.*, 2019, 29, 1904961.
51. D. Chen, J. H. Wang, T. F. Chou, B. Zhao, M. A. El-Sayed and M. Liu, Unraveling the Nature of Anomalously Fast Energy Storage in T-Nb<sub>2</sub>O<sub>5</sub>, *J. Am. Chem. Soc.*, 2017, 139, 7071-7081.
52. J. Meng, Q. He, L. Xu, X. Zhang, F. Liu, X. Wang, Q. Li, X. Xu, G. Zhang, C. Niu, Z. Xiao, Z. Liu, Z. Zhu, Y. Zhao and L. Mai, Identification of Phase Control of Carbon-Confined Nb<sub>2</sub>O<sub>5</sub> Nanoparticles toward High-Performance Lithium Storage, *Adv. Energy Mater.*, 2019, 9, 1802695.
53. Y. Li, H. Wang, L. Wang, Z. Mao, R. Wang, B. He, Y. Gong and X. Hu, Mesopore-Induced Ultrafast Na<sup>+</sup>-Storage in T-Nb<sub>2</sub>O<sub>5</sub>/Carbon Nanofiber Films toward Flexible High-Power Na-Ion Capacitors, *Small*, 2019, 15, e1804539.
54. F. Liu, X. Cheng, R. Xu, Y. Wu, Y. Jiang and Y. Yu, Binding Sulfur-Doped Nb<sub>2</sub>O<sub>5</sub> Hollow Nanospheres on Sulfur-Doped Graphene Networks for Highly Reversible Sodium Storage, *Adv. Funct. Mater.*, 2018, 28, 1800394.
55. Y. Lian, D. Wang, S. Hou, C. Ban, J. Zhao and H. Zhang, Construction of T-Nb<sub>2</sub>O<sub>5</sub> nanoparticles on/in N-doped carbon hollow tubes for Li-ion hybrid supercapacitors, *Electrochim. Acta*, 2020, 330, 135204.